PROCEEDINGS, 49th Workshop on Geothermal Reservoir Engineering
Stanford University, Stanford, California, February 12-14, 2024
SGP-TR-227

Structural and Dissolution Trapping of Carbon in Geothermal Reservoirs: A Numerical Assessment

Dale Emet Altar*, Eylem Kaya and Sadiq J. Zarrouk

Department of Engineering Science, University of Auckland, Private Bag 92019, Auckland, New Zealand

*dalt507@aucklanduni.ac.nz

Keywords: CO_2, reinjection, trapping, numerical modelling

ABSTRACT

As global policy undergoes a transformative shift towards a net-zero carbon future, there is growing interest in reinjecting non-condensable gases, including carbon dioxide, hydrogen sulfide, and methane, from geothermal power plants back into reservoirs for safe and long-term storage. Although these gases are released during power generation, the emissions are significantly lower (e.g. over 85% less in New Zealand) compared to fossil fuel power plants. Reinjection of these gases by compression and dissolution into reinjected fluids from geothermal plants (i.e. brine and condensate) presents an opportunity to ensure net-zero operations. In New Zealand, 100% gas reinjection tests have been underway in the NgāTamariki Power Station in one of its four OEC units since 2021. Similarly, Ngawha Generation has been trialling reinjection for one of its OEC units since 2022, with plans to expand across its stations. Trials are also ongoing in the Te Huka Power Station since late 2022.

Carbon dioxide capture and reinjection come with key technological and process challenges and potential reservoir management risks. These factors need careful assessment during the technology testing phase and in terms of long-term resource performance. In this study, we utilise numerical models to assess the carbon storage potential in a hypothetical geothermal reservoir and the possible risks, e.g. breakthrough and surface leakage.

1. INTRODUCTION

In the context of the evolving global commitment towards achieving a net-zero carbon future, reinjection of non-condensable gases (NCG), such as CO_2, H_2S, and CH_4, emerges as a pivotal approach for ensuring sustainable and environmentally responsible geothermal operations. Particularly, the reinjection of these gases after dissolving in waste geothermal water -comprising brine and condensate- holds the promise of facilitating net-zero operations. New Zealand has embarked on significant endeavours in this concept. Ongoing NCG reinjection trials at the Ngā Tamariki Power Station and Ngawha Generation, initiated in 2021 and 2022 respectively, underscore the practical exploration of these concepts. Additionally, the Te Huka Power Station has joined the trials in late 2022 (McLean et al., 2023). Within this transformative environment, detailed reservoir modelling studies can create an important framework for assessing the efficiency, feasibility, and long-term implications of CO_2 reinjection strategies, and contributes to the broader efforts on sustainable geothermal energy practices.

CO_2, upon injection, may be stored in a reservoir in four ways: direct physical trapping in its supercritical or gaseous phase ("structural trapping"), dissolved in the reservoir fluids ("dissolution trapping"), conversion to carbonate minerals upon reaction with the reservoir fluids and minerals ("chemical trapping") (Audigane et al., 2005), and residual trapping. However, aside from storage potential, technological and process challenges and reservoir management risks must be carefully assessed. Possible resource management risks during the testing phase and in terms of long-term resource performance include breakthrough and surface leakage (Kaya and Zarrouk, 2017; Kaya et al., 2018; Erol et al., 2022). Geothermal production may likewise be impacted by the effect of CO_2 on the fluid characteristics and reservoir pressure.

This study uses numerical models specifically developed to assess the carbon storage potential within a representative geothermal reservoir. A reservoir flow model that considers critical parameters like reservoir permeability, fluid production and reinjection rates, and CO_2 reinjection rates to predict the behaviour of the injected CO_2 within the system was used. The production of geothermal fluids was modelled along with brine and steam condensate reinjection for 40 years of field operations in a typical flash plant. Brine and condensate that are reinjected back into the reservoir contain fractions of the produced CO_2. This type of NCG reinjection is known as "passive NCG reinjection". In contrast, when supplementary energy and processes are utilised to dissolve additional gases in the reinjected fluids, it is referred to as "active NCG reinjection" (Castillo Ruiz et al., 2021). Both types were modelled in the field operations phase of the study. The models were then extended for an additional 960 years (for a total of 1000 years) without production or injection to assess the long-term storage potential in the theoretical reservoir. Sensitivity analyses explore the impact of various parameters on the reservoir performance.

2. TRANSPORT MODEL

The models were set up using the numerical simulation tool TOUGH2 (Pruess et al., 2012), utilising the EOS2 equation of state module. EOS2 provides fluid properties for binary water and CO_2 solutions for applications in gas-rich reservoirs (Pruess et al., 2012). PyTOUGH

(Croucher, 2011, 2015; Wellmann et al., 2012, 2014) was used to automate the creation and editing of model grids and data files, in grid visualisation, and model run automation. TIM (Yeh et al., 2013) was likewise used for model visualisation.

2.1. Transport Parameters

The 3D reservoir model used in this study features a grid structure covering a total area of 34 km × 28 km with a depth of 6 km (Figure 1 and Figure 2), set up following the methodology of Altar et al. (2023). To achieve a more detailed resolution in the production and injection zones, the model includes refinement at the inner blocks, utilising a grid block size of 500 m × 500 m.

Eight rock types were used for the natural state model, representative of geological structure, their stratigraphic positions, and petrophysical properties. All rock types were uniformly assigned the same grain density (2600 kg/m^3), porosity (10%), thermal conductivity (1.5 W/m-°C), and rock grain-specific heat capacity (900 J/kg-°C) as a simplifying assumption.

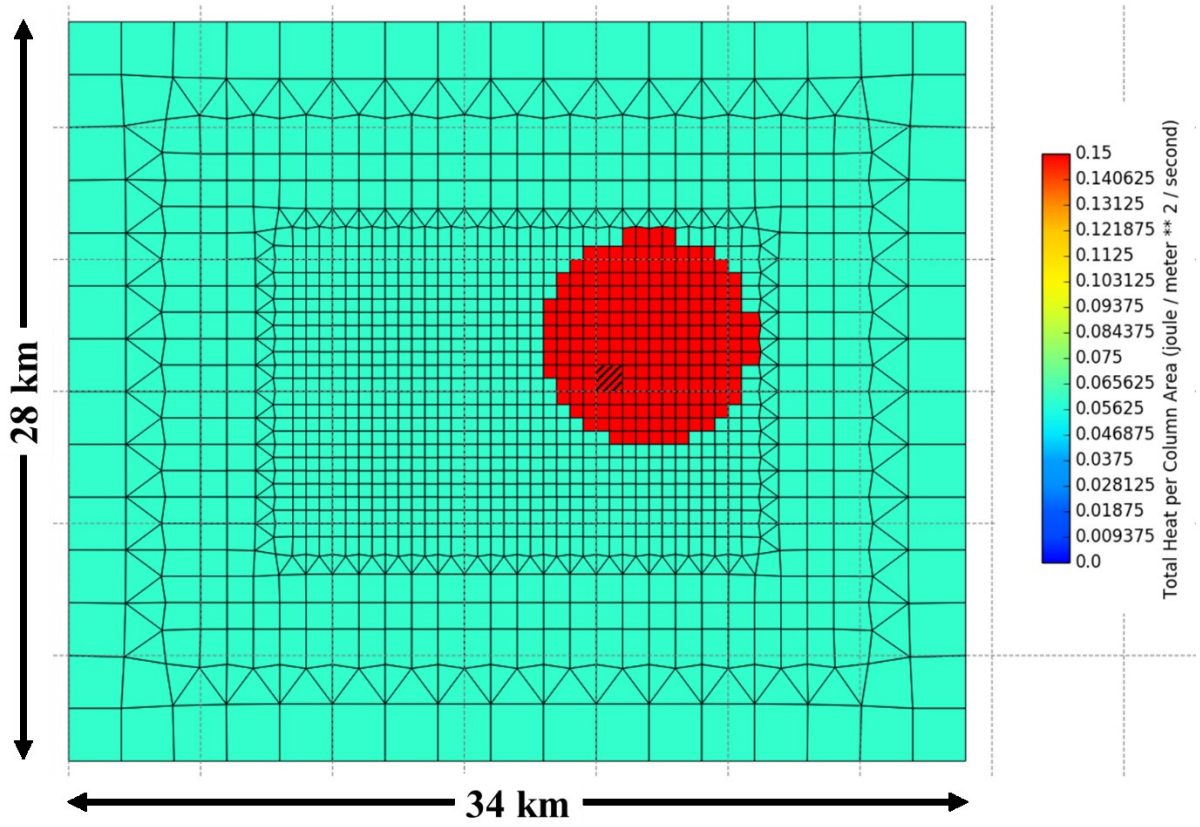

Figure 1. The bottom layer of the model grid structure. Colours represent the heat fluxes (W/m^2). The red circular area has a higher heat flux, representing the underlying heat source. Hatched red area indicates the position of the mass upflow, covering four adjacent grid blocks.

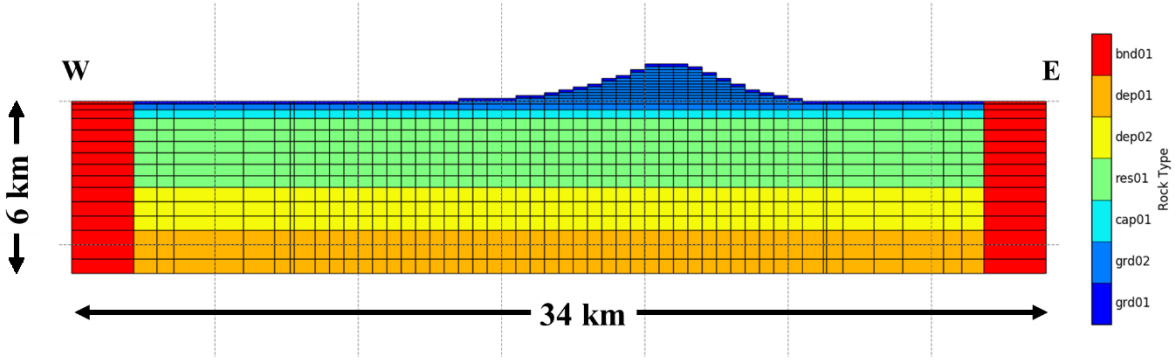

Figure 2.W-E Slice view of the model grid structure indicating the rock types.

Heat generators were added to all blocks in the bottom layer of the grid, using a baseline heat flux of 0.06 W/m^2 (Jaupart et al., 2007; Davies and Davies, 2010), and a higher value of 0.15 W/m^2 for an 8 km diameter area overlaying the geothermal system's heat source (red area in Figure 1).

Initial conditions for the model prior to analytical runs were set up following the procedure discussed in Altar (2024). The side boundary blocks were assigned volumes of $\geq 10^{50}$ m^3 to define constant boundaries for the model, ensuring that they maintain their temperatures and pressures at the initial conditions.

The model was then run to reach a stable natural state prior to running analytical scenarios. Upflow rates for both water and CO_2 were specified for natural state modelling, assigned to four adjacent blocks as indicated in Figure 1. The reservoir fluid was assumed to have the same dissolved CO_2 content as that used in Altar (2024), equivalent to a mass fraction of the total flow of 0.00062 (0.014 mol/kg). Values for the mass flow rates and enthalpies are provided in Table 1. For CO_2, the enthalpy value was determined based on the temperature and pressure values, adopted from Span and Wagner (1996).

Table 1. Mass flow rate and enthalpy of the modelled upflows per block.

Component	Mass Flow Rate, kg/s	Enthalpy, kJ/kg
Water	25	1300
CO_2	0.0154	138.5

Geothermal fluids were produced from four grid blocks positioned at a depth of 1200 m BSL. Brine and condensate resulting from the production process were reinjected at grid blocks located at 1600 m BSL depth, approximately 2 km horizontal distance away from the production blocks. Their locations are indicated in Figure 3. Production from each block was modelled using the DELV generators so that production over time is a function of well deliverability and reservoir pressure. The DELV generators require input values for the productivity index (*PI*, m^3), bottomhole pressure (Pa) and layer thickness (m).

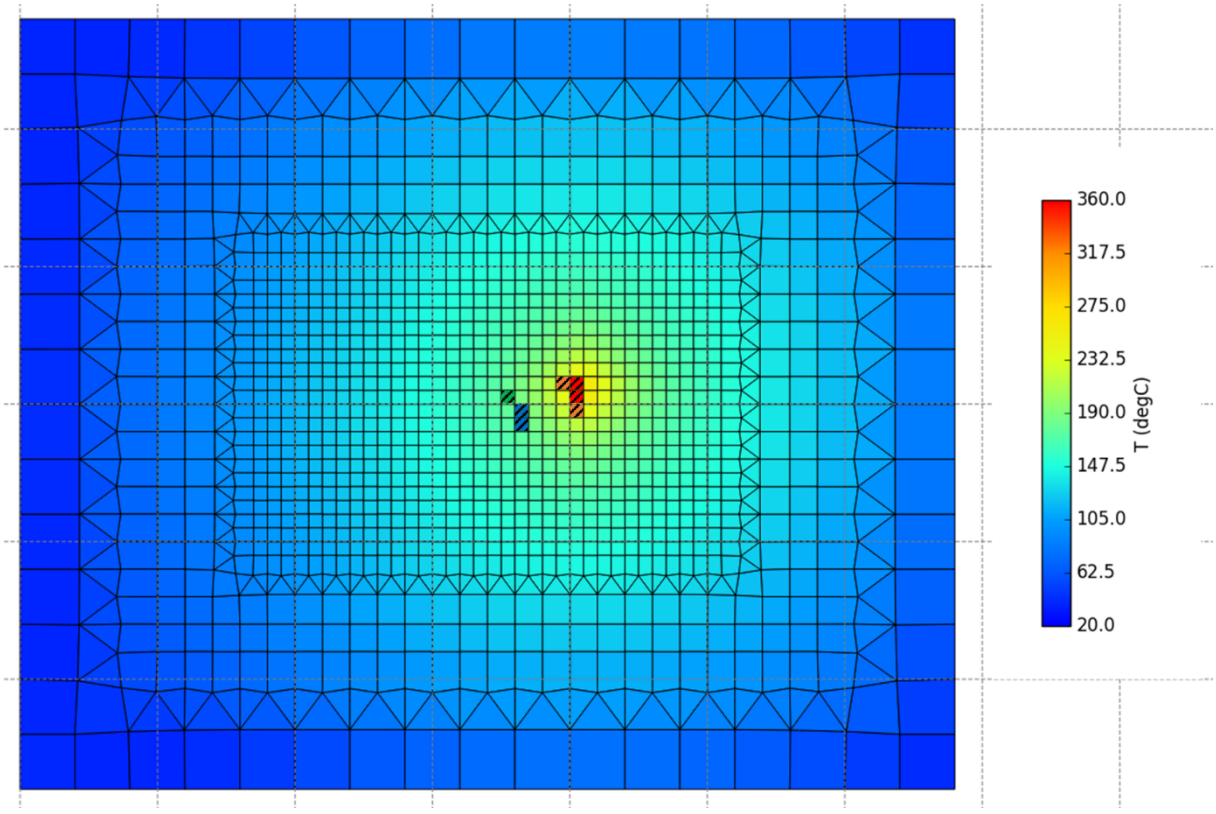

Figure 3. Model layer at 1200 m depth. Colours represent the block temperatures. Hatched red and orange areas indicates where fluids are being produced. Hatched green area indicates the condensate injection block location, while the hatched blue areas correspond to the brine injection blocks, all of which are at 1600 m depth.

The productivity index was estimated using Eqn (1) from Pruess et al. (2012),

$$PI = \frac{2\pi(k\ \Delta z)}{ln\left(\frac{r_e}{r_w}\right) + s - \frac{1}{2}} \quad (1)$$

where k is permeability (m^2), Δz is the layer thickness (m), r_e is the grid block radius (m), r_w is the well radius (m) and s is the skin factor (dimensionless). Since the grid blocks are rectangular and not cylindrical, the value for r_e may be computed as the effective radius using Eqn (2). Here, A is the area of the block along the x-y plane in m^2.

$$r_e = \sqrt{\frac{A}{\pi}} \quad (2)$$

The refined blocks are 500 m × 500 m, with a corresponding grid block radius of 282.1 m. The remaining variables for calculating the productivity index are summarized in Table 2. A productivity index of 4.72 × 10^{-12} m^3 was calculated from the variables provided. The well radius value assumes that the production liners have a diameter of 9 5/8" (244.5 mm) with a nominal weight of 47lb/foot. No skin effects were considered (s = 0).

Table 2. Variables for the computation of productivity index in the flow model.

Variable	Condensate
k, m^2	5.00E-14
Δz, m	100
A, m^2	2.50E+05
r_e, m	282.1
r_w, m	0.2205
s	0

Using the calculated productivity index, TOUGH2 calculates the mass production rate through Eqn (3) from Pruess et al. (2012).

$$q_\beta = \frac{k_{r\beta}\rho_\beta}{\mu_\beta} PI\left(P_\beta - P_{wb}\right) \quad (3)$$

Here q is the mass generation rate (kg/s), k_r is relative permeability (dimensionless), ρ is density (kg/m^3), μ is dynamic viscosity (Pa·s), P_{wb} is the wellbore pressure (Pa), and P is the block pressure (Pa), while the subscript β pertains to each fluid phase present.

The final variable needed is the wellbore pressure, which was estimated using wellbore simulations. Production wells were assumed to be vertical with a total depth of 1800 m. The upper casing was taken to be 13 3/8" (339.7 mm) in diameter with a nominal weight of 54.5lb/foot, spanning from ground level (600 m ASL) to 600 m BSL. The remaining wellbore section corresponds to the 9 5/8" production liner. An iterative calculation was carried out to estimate the bottom hole pressure as there is a feedback effect from the mass produced from each block to the calculated wellbore pressure, depending on the block pressure and enthalpy. The calculations resulted in two representative values for the bottom hole pressures corresponding to the blocks marked in red (1140 kJ/kg, 136 bar) and orange (1030 kJ/kg, 136 bar) in Figure 3; 110 bar and 88 bar, respectively.

From the steamfield process perspective, a single flash process with a separation pressure of 5.5 bar was considered. The separated steam is converted to electrical power in a power plant, while the separated brine is reinjected. Condensed steam from the turbines is pumped to a cooling tower before reinjection. This process was used to calculate the corresponding injection rate profiles over time. A simplifying assumption of this analysis is that heat losses from the fluid transport system are negligible and that processes are adiabatic. For a given two-phase fluid mass rate m_{2ph} (kg/s) with enthalpy h_{2ph} (kJ/kg), the corresponding steam and brine mass rates (m_{steam} and m_{brine}, kg/s) leaving the separator are calculated using Eqn (4), (5) and (6)

$$x = \frac{h_{2ph} - h_{liq,sep}}{h_{vap,sep} - h_{liq,sep}} \quad (4)$$

$$m_{steam} = x m_{2ph} \quad (5)$$

$$m_{brine} = (1 - x) m_{2ph} \quad (6)$$

where $h_{liq,sep}$ and $h_{vap,sep}$ are the saturated liquid and vapor enthalpies of water at the separation pressure, and x is the steam fraction. These calculations were completed for each production profile over time resulting from the four production blocks in the model. The total of all brine rates was divided evenly between the two brine injection blocks.

For condensate injection, a factor of 20% was multiplied to the total steam rate to approximate condensate injection rates. The proportion factor was based on operations experience for a similar steamfield process design.

Brine and condensate injection profiles were input in the model as tables of generation rate versus time. The production and injection rates are plotted in Figure 4. Note the steep decline in production within the first year, and how a significant portion of the produced fluids are simply reinjected as brine and not used for power generation.

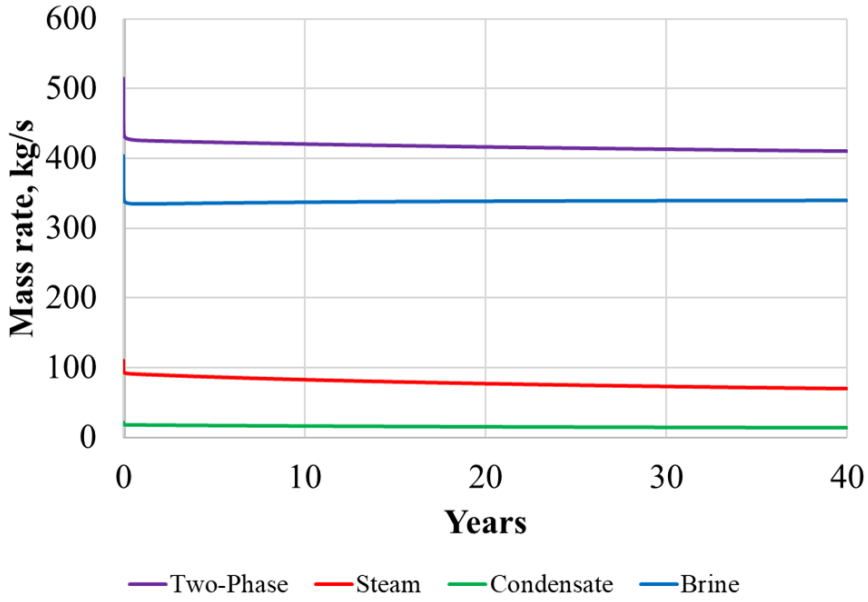

Figure 4. Total two-phase fluid production, steam and injection rates for brine and condensate over time.

CO_2 mass generators were also added to the injection blocks, corresponding to the amount of dissolved gas in the reinjected fluid. For the passive reinjection case, the equivalent mass fractions in the injectates are 0.00028 (0.0064 mol/kg) and 0.000036 (0.00082 mol/kg) for brine and condensate, respectively. The details of the chemistry of the brine and condensate used in the study are provided in Altar (2024).

Values for the CO_2 enthalpies are provided in Table 3, along with the corresponding temperature and pressure conditions. The brine was assumed to be at saturated liquid conditions at the separator pressure, while the condensate was at a temperature of 25°C under 1 bar pressure (atmospheric pressure conditions).

Table 3. CO_2 enthalpy values (Span and Wagner, 1996) and the corresponding temperature and pressure conditions for the passive NCG reinjection scenario.

	Brine	Condensate
Temperature, °C	155.5	25
Pressure, bar	5.5	1
Enthalpy, kJ/kg	115.9	-0.93

For the active NCG reinjection scenarios, 20 bar and 40 bar injection pressures were selected. In all cases, the carrier fluid is taken to be fully saturated with dissolved CO_2 at the given pressure and injectate temperature. To simplify the analysis, the solution only considers water and CO_2. The first step in estimating the amount of dissolved CO_2 at saturated conditions involves Henry's Law, Eqn (7).

$$P_{gas} = K_{Hb} x_{gas,aq} \tag{7}$$

According to Henry's Law (Pruess et al., 2012), the partial pressure of a gas in the vapor phase of a solution (P_{gas}, Pa) is equal to the product of its mole fraction in the aqueous phase ($x_{gas,aq}$, dimensionless) multiplied by the Henry's law coefficient for the gas (K_{Hb}, Pa).

The Henry's law coefficient for CO_2 is dependent on temperature and the ionic strength of the solution. For this study, the formulation for K_{Hb} by Battistelli et al. (1997), Eqn (8), (9) and (10), was used to estimate the amount of CO_2 in the saturated solutions, the same formulation used for EOS2 in TOUGH2.

$$K_{Hb} = K_H 10^{|mk_b|} \tag{8}$$

$$K_H = \sum_{i=0}^{5} B_{(i)} T^i \tag{9}$$

$$k_b = \sum_{i=0}^{4} C_{(i)} T^i \tag{10}$$

In these equations, K_H is the Henry's law coefficient as a function of temperature for pure water (Pa), k_b is the salting out coefficient, m is salt molality (mol/kg), which is equivalent to the ionic strength of the aqueous phase, $B_{(i)}$ and $C_{(i)}$ are coefficients reported by Battistelli et al. (1997), and T is temperature (°C).

The partial pressure of water as the solvent also needed to be considered. The partial vapor pressure of water may be estimated using Raoult's Law which takes a form very similar to Henry's Law,

$$P_{solvent} = P^*_{solvent} x_{solvent} \tag{11}$$

In Eqn (11), the partial pressure of the solvent in the vapor phase ($P_{solvent}$, Pa) is a product of the vapor pressure of the pure solvent ($P^*_{solvent}$, Pa) and the mole fraction of the solvent in the aqueous solution ($x_{solvent}$). Both Henry's and Raoult's laws apply under equilibrium conditions between the aqueous and vapor phases, therefore for a binary solution of CO_2 in water to be saturated, it must follow the condition given by Eqn (12).

$$P_{total} = P_{H_2O} + P_{CO_2} = P^*_{H_2O} x_{H_2O} + K_{Hb,CO_2} x_{CO_2} \tag{12}$$

The results of the above calculations are summarized in Table 4 along with the corresponding enthalpy values for CO_2. The solubility of gases tends to decrease with increasing temperature, which can be observed in the mole fractions of CO_2 dissolved in the brine and condensate for the same pressure conditions. Similarly, the tendency for gas solubility to increase with pressure may be noted from the calculated values.

Table 4. CO_2 mole fractions in solution and enthalpy values (Span and Wagner, 1996) for the temperature and pressure conditions used in this study for the active NCG reinjection scenarios.

		P = 20 bar		P = 40 bar	
Fluid	Temperature, °C	x_{CO2}	Enthalpy, kJ/kg	x_{CO2}	Enthalpy, kJ/kg
Brine	155.5	0.0022	109.4	0.0052	100.4
Condensate	25	0.0118	-20.3	0.0236	-46.6

2.2. Model Scenario Descriptions

The NCG reinjection scenarios involve various combinations of CO_2-loading in the reinjected fluids (Table 5). All model scenarios involved an initial 40 years of concurrent production and reinjection, after which production ceased, and the models were run for an additional 960 years to track how the sequestered CO_2 behaves over time.

Table 5. Scenario descriptions for Phase 1 of the study. Notations indicate the amount of dissolved CO_2: B for baseline, S for saturated at the given dissolution pressure.

Scenario	Gas Dissolution Pressure, bar	Brine	Condensate
Baseline		B	B
20-B	20	S	B
20-C		B	S
20-BC		S	S
40-B	40	S	B
40-C		B	S
40-BC		S	S

3. RESULTS AND DISCUSSIONS

The mass rates of reinjected CO_2 over time are presented in Figure 5. From the historical profiles, the cumulative masses of injected CO_2 (m_{CO2}, tonnes) were calculated using Eqn (13), where q_{CO2} is the CO_2 mass rate (kg/s) and Δt are incremental time step lengths (s).

$$m_{CO_2} = \frac{1}{1000}\sum(q_{CO_2}\Delta t) \tag{13}$$

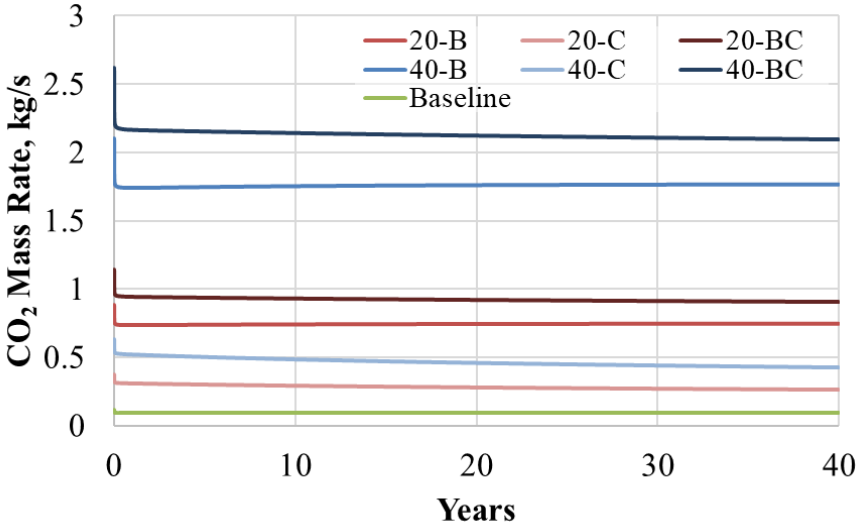

Figure 5. CO_2 mass injection profiles for the scenarios.

The total injected CO_2 mass from the passive NCG reinjection scenario is approximately 1.20×10^5 tonnes. Subtracting this amount from the masses calculated for each scenario results in the values for the incremental CO_2 injection from each of the scenarios.

The data was visualised within a 10 km × 8 km × 4 km region of the reservoir which includes the production and injection blocks and their peripheries. Both the top view of the 1200 m layer and a slice view intersecting the condensate injection block and one production block are shown in Figure 6. A dashed line on the top view indicates where the slice view is located. The red hatched areas indicate the production blocks. The blue and green hatched areas correspond to the locations of the brine and condensate injection blocks at a depth of 1600 m.

Table 6. Incremental masses of CO_2 injected into the reservoir for each scenario relative to the baseline.

Scenario	Incremental CO_2 Injection, 10^5 tonnes
20-B	8.14
20-C	2.32
20-BC	10.46
40-B	21.02
40-C	4.65
40-BC	25.67

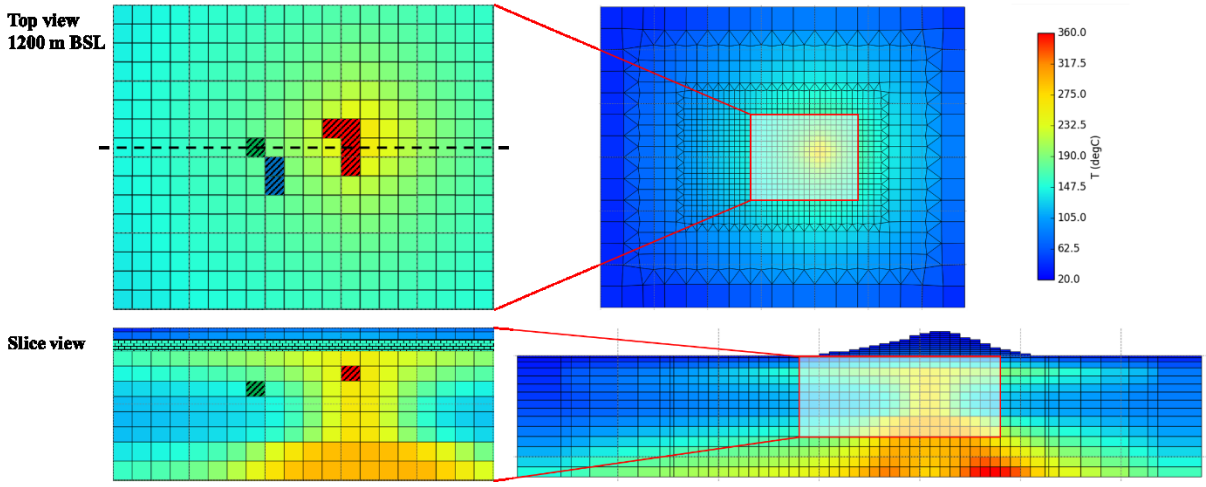

Figure 6. Top view at 1200 m BSL and slice view of the region of interest in the modelled reservoir.

The results of scenarios 20-B, 20-C and 20-BC after 40 years are shown in Figure 7. For scenario 20-B, the trend for the movement of injected CO_2 indicates that brine injection returns to the production area over time. In contrast, the CO_2 reinjected with the condensate tends to migrate away from the production area (scenario 20-C). This behaviour is driven by the movement of the reinjected brine. Higher brine injection rates cause a sweeping effect driving reinjected condensate away from the production area. Both behaviours become apparent when both the brine and condensate are enriched with CO_2, as observed in scenario 20-BC.

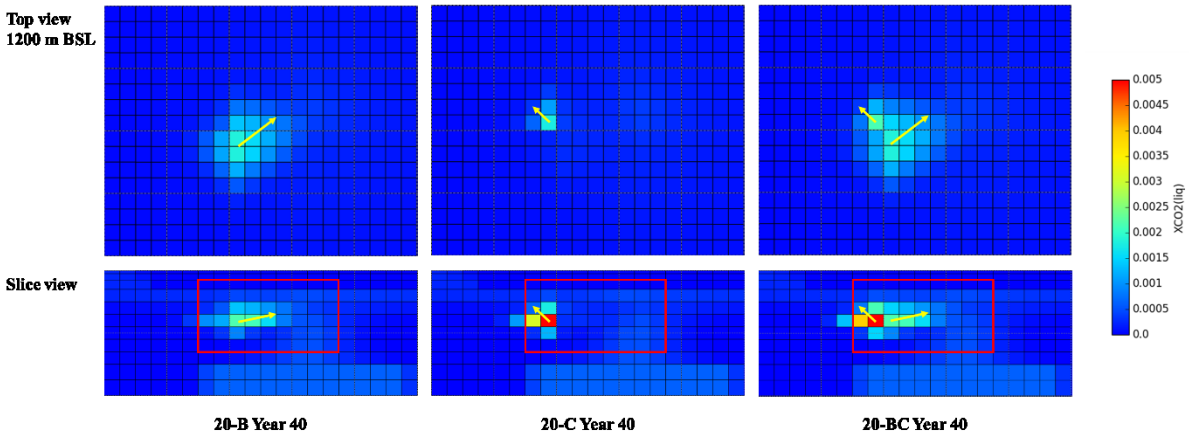

Figure 7. Top view and slice view of the region of interest showing the CO_2 mass fractions at Year 40 for the 20-B, 20-C and 20-BC scenarios. Yellow arrows indicate overall flow direction of injected CO_2.

The effects to total mass production rates and total production enthalpy were found to be negligible for all three scenarios relative to the baseline. However, CO_2 concentrations in the produced fluids increased, particularly for scenarios 20-B and 20-BC. The results are plotted in Figure 8. For the 20-C scenario, no CO_2 returns were observed, while both 20-B and 20-BC result in near identical return trends.

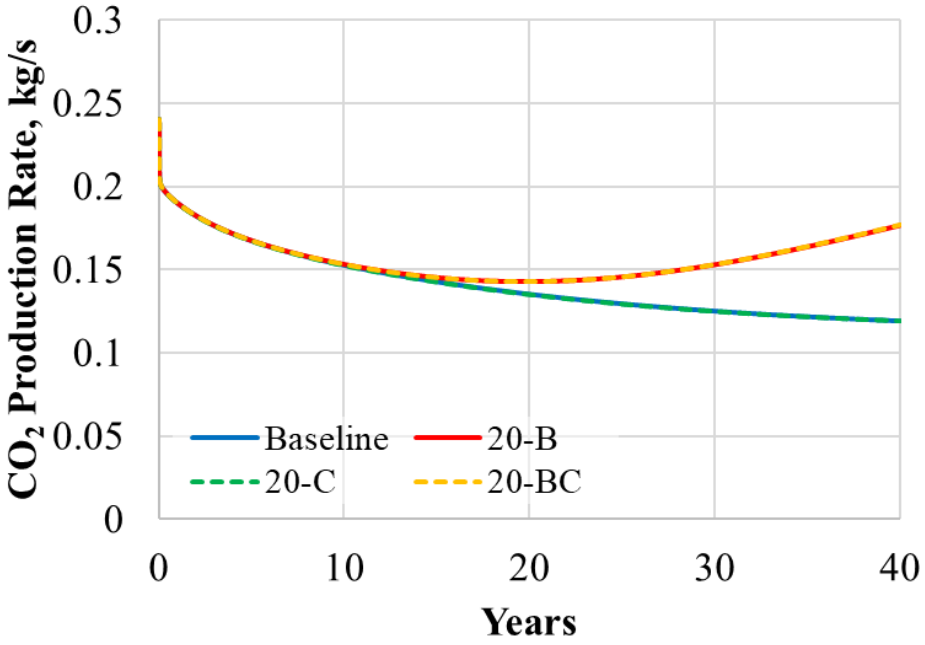

Figure 8. CO_2 mass fractions in the produced fluids for the 20 bar scenarios and the baseline.

Using Eqn (13), the total CO_2 mass produced for the latter two scenarios is 1.98×10^5 tonnes over 40 years, compared to 1.78×10^5 tonnes for the baseline, a 0.20×10^5 tonne increase over 40 years. Due to the returns, the effective total mass of CO_2 stored in the reservoir reduced to 7.94×10^5 tonnes and 10.26×10^5 tonnes for the 20-B and 20-BC scenarios, respectively, meaning that storage efficiency, when using brine as the carrier fluid, ranges from 97.5% to 98.1% for the theoretical reservoir.

Within the 40-year production period, no surface leakage was observed for the reservoir conditions defined. Further changes in the reservoir CO_2 after production ceased were reviewed. For this, only scenario 20-BC was considered. The results are illustrated in Figure 9.

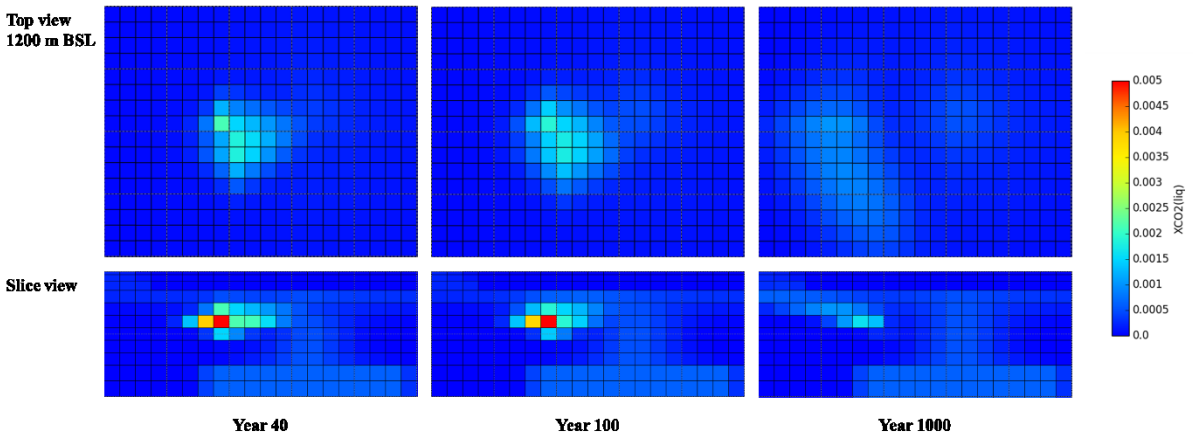

Figure 9. Top view and slice view of the region of interest showing the CO_2 mass fractions after 100 years and 1000 years for the 20-BC scenario.

Within 1000 years, dispersion of the injected CO_2 is evident, attributed to diffusion and bulk mass transfer due to fluid circulation. There were no instances of rapid transport to the surface observed. However, long-term storage could not be verified with practical certainty because of the large quantities of mass in place. To clarify, prior to any model runs, the total CO_2 already in place are in magnitudes of 10^{45} kg, compared to the 10^8 to 10^9 kg of injected mass.

The same analytical steps were prepared for the 40 bar injection pressure scenarios. The modelled behaviour of the 40-B scenario was found to be consistent with that of 20-B, 40-C relative to 20-C, and 40-BC to 20-BC. Therefore, the following discussion will primarily focus on the results of 40-BC.

The higher CO_2 concentrations for the 40 bar injection scenarios resulted in increased production returns when co-injected with brine (Figure 10). Returns were not observed for the 40-C scenario, whereas comparable returns are noted for 40-B and 40-BC.

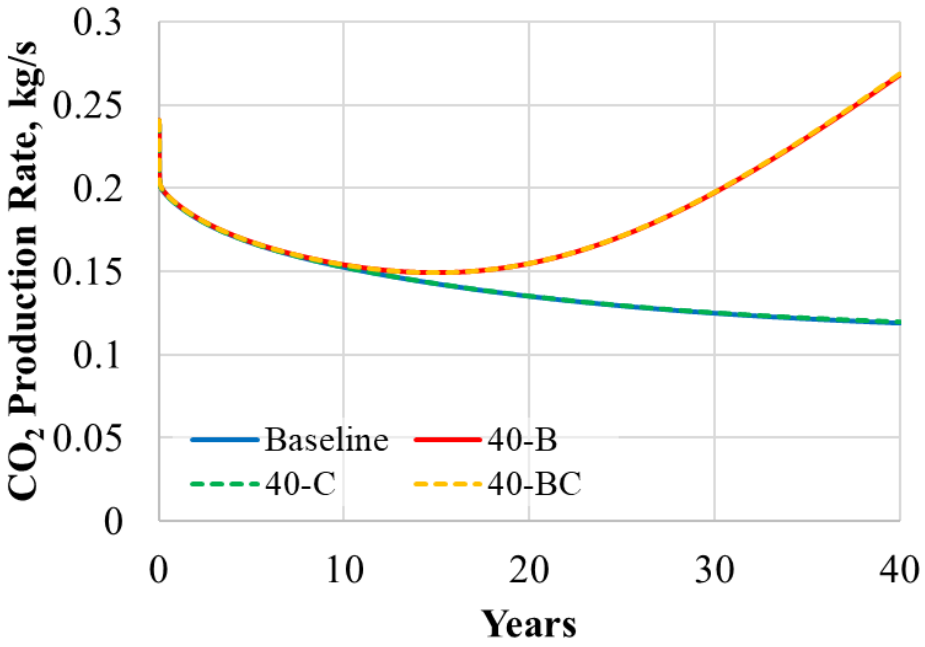

Figure 10. CO_2 mass fractions in the produced fluids for the 40 bar scenarios and the baseline.

The total CO_2 mass produced from 40-B and 40-BC is 2.29×10^5 tonnes over 40 years, a 0.51×10^5 tonne increase compared to the baseline production scenario. From this, the net CO_2 mass input into the reservoir for the 40-B and 40-BC scenarios are 20.51×10^5 tonnes and 25.16×10^5 tonnes, respectively. This is equivalent to an injection efficiency of 97.6% to 98.0% over 40 years when using brine as carrier fluid. These numbers are very similar to those evaluated from the 20 bar injection scenarios.

Surface leakage was not observed during the 40-year production period for the reservoir conditions defined. The CO_2 concentrations in the blocks affected by injection progressively decreased over 1000 years, and model results indicate that the dissolved gases are being transported by the convection currents within the reservoir. (Figure 11 and Figure 12).

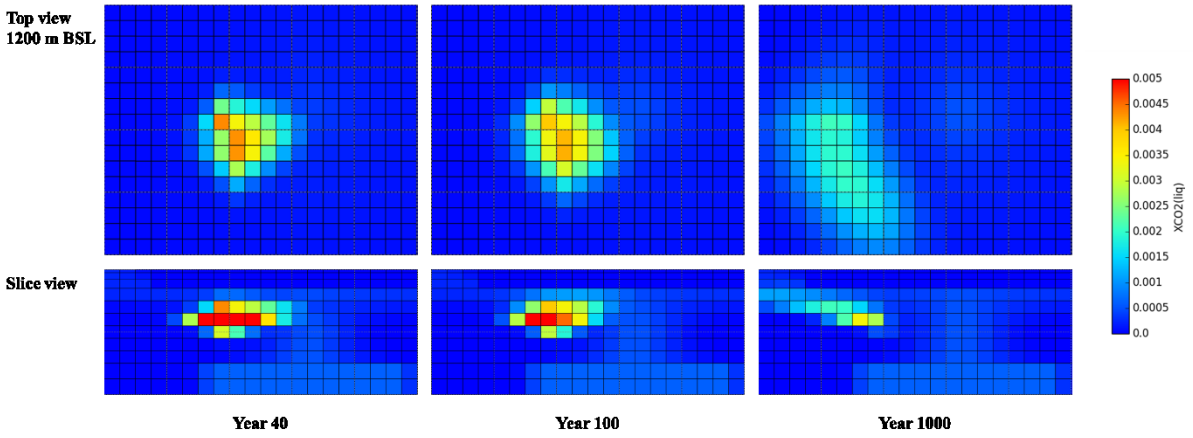

Figure 11. Top view and slice view of the region of interest showing the CO_2 mass fractions after 100 years and 1000 years for the 40-BC scenario.

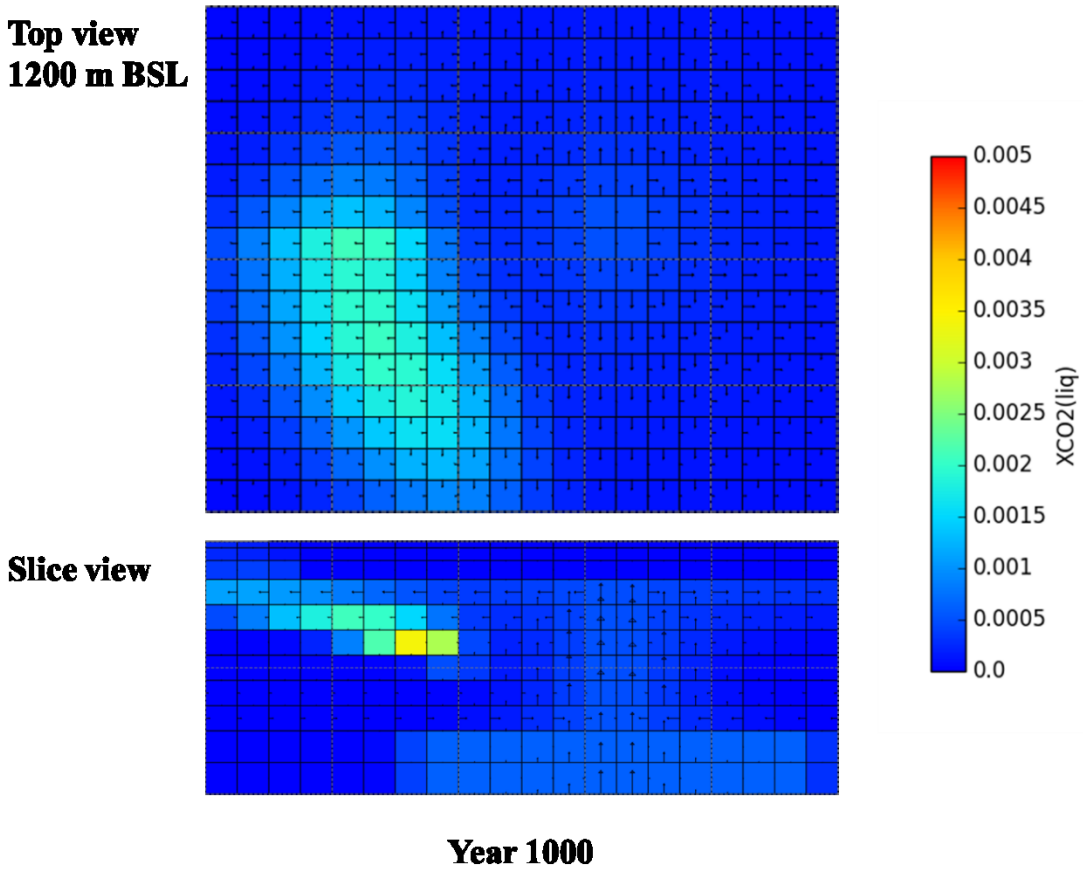

Figure 12. Top view and slice view of the region of interest showing the CO_2 mass fractions after 1000 years for the 40-BC scenario, with arrows indicating the fluid flow paths within the reservoir.

CO_2 remained in solution in all scenarios modelled. Structural trapping capacity could not be verified as CO_2 was not observed as a separate phase. The injected CO_2 was effectively stored within the modelled reservoir through the dissolution trapping mechanism, and no surface leakage was observed.

4. CONCLUSIONS

The results of the study showed that carbon storage in a geothermal reservoir is feasible. Two mechanisms were considered for the investigation: structural trapping and dissolution trapping. Results showed that more than 99% of injected CO_2 for sequestration is trapped through dissolution. Structural trapping was not observed as CO_2 did not exist as a separate phase in the modelled reservoir.

It was observed within 1000 years that the injected CO_2 were dispersed throughout the reservoir by convection currents. In a reservoir with no preferential pathways to the surface through which the reinjected CO_2 may leak in appreciable amounts, sequestered CO_2 may still be gradually released over time through the transport of reservoir fluids. A practical method to ascertain this was not available at the time of this investigation and should be considered in future work.

Depending on the connectivity of the reinjection and production sectors, injected CO_2 may communicate and be produced with steam or two-phase fluids. This risk decreases the efficiency of the process and should be considered in future work. Other impacts related to reservoir pressure, fluid enthalpy and productivity should likewise be analysed, though they were not observed in the modelled reservoir for this study.

Future studies should assess the effects of other NCGs, e.g., H_2S, O_2, and N_2, which may be present with CO_2 and can affect the evolution of fluid chemistry and the mode of mineral alteration. Longer term model runs and structural influences on reservoir flow path behaviour should also be incorporated to investigation scenarios.

ACKNOWLEDGEMENTS

This work was supported by the University of Auckland Doctoral Scholarship. We also thank the NZ Ministry of Business, Innovation and Employment for funding the work through MBIE Research Programme: UOAX2211 "Reversing Carbon Emissions in the Geothermal Energy Industry: Template for Emission-Intensive Industries" projects.

REFERENCES

Altar D.E. (2024), Reactive Transport Modelling of Flow Through Porous and Fractured Media in Geothermal Systems, PhD thesis, University of Auckland

Altar D.E., Zarrouk, S. and Kaya, E. (2023), Understanding Mineralogical and Geochemical Evolution in Geothermal Reservoirs through Reactive Transport Modelling, Proceedings 45th New Zealand Geothermal Workshop, 15-17 November, 2023, Auckland, New Zealand, ISSN 2703-4275

Audigane, P., Gaus, I., Pruess, K., Xu, T., 2005. Reactive transport modeling using TOUGHREACT for the long term CO2 storage at Sleipner, North Sea. In: Proceedings, 4th Annual Conference on Carbon Capture and Sequestration DOE/NETL

Battistelli, A., Calore, C., Pruess, K., 1997. The simulator TOUGH2/EWASG for modelling geothermal reservoirs with brines and non-condensible gas. Geothermics 26 (4), 437-464

Castillo Ruiz, N., McLean, K., Richardson, I., Misa, T., Ferguson, A., Altar, D., Kaya, E., 2021. Passive NCG Reinjection at Te Huka Geothermal Binary Power Plant. In: Proceedings, 43rd New Zealand Geothermal Workshop. Wellington, New Zealand

Croucher, A.E., 2011. PyTOUGH: a Python scripting library for automating TOUGH2 simulations. In: Proceedings, New Zealand Geothermal Workshop 2011. Auckland, New Zealand

Croucher, A., 2015. Recent developments in the PyTOUGH scripting library for TOUGH2 simulations. In: Proceedings, 37th New Zealand Geothermal Workshop. Taupo, New Zealand

Davies, J.H., Davies, D.R., 2010. Earth's surface heat flux. Solid earth 1 (1), 5-24

Erol, S., Akın, T., Başer, A., Saraçoğlu, Ö, Akın, S., 2022. Fluid-CO2 injection impact in a geothermal reservoir: Evaluation with 3-D reactive transport modeling. Geothermics 98, 102271. https://doi.org/10.1016/j.geothermics.2021.102271

Jaupart, C., Labrosse, S., Lucazeau, F., Mareschal, J.C., 2007. 7.06-temperatures, heat and energy in the mantle of the earth. Treatise on geophysics 7, 223-270

Kaya, E., Callos, V., Mannington, W., 2018. CO2 –water mixture reinjection into two-phase liquid dominated geothermal reservoirs. Renewable Energy 126, 652-667. https://doi.org/10.1016/j.renene.2018.03.067

Kaya, E., Zarrouk, S.J., 2017. Reinjection of greenhouse gases into geothermal reservoirs. International Journal of Greenhouse Gas Control 67, 111-129. https://doi.org/10.1016/j.ijggc.2017.10.015

McLean, K., Montague, T., Alcaraz, S., Daysh, S., Doorman, P., Luketina, K., Tsui, K., White, B., Zarrouk, S.J., 2023. 2020-2023 New Zealand Country Update. In: Proceedings, World Geothermal Congress 2023

Pruess, K., Oldenburg, C.M., Moridis, G.J., 2012. TOUGH2 User's Guide Version 2. Lawrence Berkeley National Laboratory

Span, R., Wagner, W., 1996. A new equation of state for carbon dioxide covering the fluid region from the triple-point temperature to 1100 K at pressures up to 800 MPa. Journal of physical and chemical reference data 25 (6), 1509-1596

Wellmann, J.F., Croucher, A., Regenauer-Lieb, K., 2012. Python scripting libraries for subsurface fluid and heat flow simulations with TOUGH2 and SHEMAT. Comput. Geosci. 43, 197-206. https://doi.org/10.1016/j.cageo.2011.10.011

Wellmann, J.F., Finsterle, S., Croucher, A., 2014. Integrating structural geological data into the inverse modelling framework of iTOUGH2. Comput. Geosci. 65, 95-109. https://doi.org/10.1016/j.cageo.2013.10.014

Yeh, A., Croucher, A.E., O'Sullivan, M.J., 2013. TIM-Yet another graphical tool for TOUGH2. In: Proceedings, 35th New Zealand Geothermal Workshop. Rotorua, New Zealand